Wake instability behind a streamwise and transversely rotating sphere

Arnab Kumar De

Department of Mechanical Engineering, Indian Institute of Technology Guwahati, Assam 781039, India

Sandip Sarkar [*]

Department of Mechanical Engineering, Jadavpur University, Kolkata 700032, India

We have performed direct numerical simulations for the flow past a streamwise and transversely rotating sphere at a Reynolds number Re = 500. To investigate the effect of low to very high rotation rates on the flow dynamics, we have varied the dimensionless streamwise (Ω_x) and transverse (Ω_z) rotation rates between 0.5 and 5. The streamwise rotation of the sphere causes twisting of the vortex structures in the wake and results in centrifugal instabilities. The wake consists of two intertwined spiral vortices at $\Omega_x = 0.5$, whereas the vortex structures form threads and bifurcate into large-scale shear layers for $\Omega_x \geqslant 2$. The shedding pattern during the transverse rotation is subject to turning. The structures at the aiding side of the motion experience tearing, whereas they squeeze at the opposing side. We found single-sided shedding of the hairpin structure at $\Omega_z = 0.5$. The wake deforms into numerous small-scale vortex filaments for $\Omega_x = 2$, whereas it becomes complex, constituting stretched hairpins at $\Omega_x = 5$. During the rotation cycle of the sphere, the wake shows steady flow at $\Omega_x = 0.5$. In contrast, at $\Omega_z = 0.5$, we found one-sided shedding of hairpin vortices in the near wake, which becomes ringlike vortices in the far wake. The wake at $\Omega_z = 2$ forms randomly oriented vorticity patches, which cannot cope with the sphere's rotation, thereby retaining their shape and orientation during the rotation cycle. The line-time reconstruction of vertical velocity signals shows discontinuity in vortex formation for higher $\Omega_{x,z}$. We have formulated a method for tracking the trajectories of the vortices. In the near wake at $\Omega_x = 0.5$, the vortex trajectories move in a circular path, whereas it settles at a larger radius in the far wake. We observe that for $\Omega_x \geqslant 2$, the local rotation center of the near-wake vortices cannot cope with high rotational speeds, and the fluid particles partially obey the effects of solid-body rotation. A higher degree of mixing of the fluid particles in the near wake at $\Omega_x = 5$ decreases the localized rotation of the vortex trajectories, and the vortex centers settle along the radial lines in the far wake. We found the symmetric distribution of the vortex trajectories at all transverse planes during Ω_z rotation. Our results indicate that a rotating sphere always experiences a positive drag irrespective of the rotational direction. The time average normalized angular velocity of the vortices at various transverse planes reveals that the near wake vortices could cope with the sphere's rotation for $\Omega_x = 0.5$. However, it decays marginally for $\Omega_x = 2$. In contrast, most of the rotational speed is lost for $\Omega_x = 5$. We have calculated the penetration depth as the downstream length for which 10% of the sphere's angular speed is preserved by the downstream vortices, which reveals rapid reduction for increasing Ω_x. At various downstream locations, the normalized angular frequency of the vortices renders the asynchronous rotation of the vortex structures. We found a minimal impact of Ω_z on the rotation of the downstream vortices. However, the wake fluctuations are triggered with increasing rotation rate, although fluctuations are lesser for Ω_z rotation. The near wake

---

[*]sandipsarkar.mech@jadavpuruniversity.in; thesandipsarkar3@gmail.com

vortices reveal low-frequency rotation for all Ω_z, and the asynchronous motion of the vortices triggers its asynchronicity for increasing Ω_z.

I. INTRODUCTION

Description of wake structure past a rotating sphere has attracted significant research attention owing to its prominent role in many engineering applications. Such applications include freely falling or rising bodies [1,2], sports aerodynamics [3,4], particle-driven flows [5], and fluidized bed combustion [6], to name a few. In addition, the rotating sphere undergoing transverse rotation has historically drawn several researchers to understand the induced "Robins-Magnus" lift force, which has several consequences on the industrial implications. Subsequently, studies on analytical framework [7] reported expression for the "Robins-Magnus" lift coefficient (C_L) in the Stokes regime (Re $\leqslant 0.1$, $\Omega \leqslant 0.1$) as $C_L = 2\Omega$. Here Re $= U_\infty D/\nu$ is the Reynolds number, D is the sphere diameter, U_∞ is the streaming speed, and ν is fluid kinematic viscosity. The dimensionless rotational speed of the sphere is given by $\Omega = D\alpha/2U_\infty$, where α is the angular velocity of the sphere perpendicular to the free stream. Interestingly, the drag coefficient has shown to be the Stokes drag of a stationary sphere [7].

The earliest known experimental work on the flow past a streamwise rotating sphere dates back to mid-1930 [8]. Later, Luthander and Ryberg [9] carried out experiments for rotating sphere flow in the range of Reynolds number $1–5 \times 10^5$. They observed that the transition from laminar to turbulent boundary layer depends on the rotation rate. Hoskin [10] noticed that the rotating motion also affects the separation line, where an increase in rotation rates causes upstream motion of the separation line by $10°$ within the laminar regime. A few experimental works have been beyond the Stokes regime, where researchers measured the lift force for a transversely rotating sphere in a uniform flow [11–13]. Recently, there have been other experimental studies for Re $\geqslant 6 \times 10^4$ focusing on the influence of transverse rotation on the inverse Magnus effect [14–16]. It has been found that an increase in Re caused a sudden change in the direction of the rotation-induced lift. In a more recent study, Skarysz *et al.* [17] experimented wake behind a rotating sphere for Re $\leqslant 500$ and $0 \leqslant \Omega \leqslant 4$. In the (Re, Ω) parameter space, they identified an axisymmetric flow, a low helical state, and a high helical mode wake regime.

From the numerical perspective, Kurose and Komori [18] performed direct numerical simulation (DNS) for a rotating sphere in a homogeneous linear shear flow in the range of $1 \leqslant$ Re $\leqslant 500$ and $0 \leqslant \Omega \leqslant 0.25$. They presented a detailed analysis of the flow structure and vortex shedding frequency. Results from their simulation showed to be in good agreement with the thereafter DNS study of Niazmand and Renksizbukut [19] for $10 \leqslant$ Re $\leqslant 300$ and $0 \leqslant \Omega \leqslant 1$. The three-dimensional (3D) numerical simulation for a streamwise rotating sphere by Kim and Choi [20] for $0 \leqslant \Omega \leqslant 1$ revealed that the flows become "frozen" at $\Omega = 0.5, 6$ for Re $= 300$. In the "frozen" state, the wake vortical structures rotate without temporal variation of their strength, and the lift force becomes a time-independent constant magnitude. They showed that the "frozen" flow becomes prevalent at higher Ω for increasing Re. Later, Kim [21] reported that the critical rotational speed for the commencement of shear layer instability is higher at Re $= 250$ than at Re $= 300$. Giacobello *et al.* [22] reported numerical results for the flow past a transversely rotating sphere for Re $\leqslant 300$ and $\Omega \leqslant 1$. The study showed wake transition over the regime of Ω considered. At $\Omega \geqslant 0.8$, the vortex shedding resembled typical shear layer instability associated with the Kelvin-Helmholtz pattern. Later research on a streamwise rotating sphere for Re $\leqslant 350$ and $\Omega \leqslant 2$ identified low-frequency periodic helical, quasiperiodic shedding, and high-frequency periodic helical wake modes [23].

A thorough numerical analysis of the flow past a transversely rotating sphere for Re $= 500–1000$ and $\Omega \leqslant 1.2$ by Poon *et al.* [24] revealed a new "shear layer-stable foci" flow regime. The flow regime stays at Re $= 500$ and $\Omega = 1$; Re $= 640–1000$ and $\Omega \geqslant 0.8$, resulting in stable focus

formation near the onset of the shear layer instability. Dobson *et al.* [25] performed simulations for a transversely rotating sphere at Re = 100–300 and Ω = 1.25–3. They found that for $\Omega > 2$, the flow enters the "separatrix" regime, which bifurcates the surface-driven boundary layer engulfing the sphere surface and the free stream flow. However, a few other important numerical studies have been conducted by the same group of researchers to examine the effect of rotating axis angle [26] and hydrodynamic forces [27] past a rotating sphere. In a contemporary research, Lorite-Díez and Jiménez-González [28] carried out DNS behind a strongly streamwise rotating sphere for $\Omega = 0$–3 and Re $\leqslant$ 1000, reported higher wake complexity for increasing Ω. The wake constitutes double-threaded structures at low Re and strong Ω. Their results have shown the evolution of periodic, quasiperiodic, and irregular regimes, comprising a classical scenario of a route to chaos at low and intermediate Re. More recently, Sierra-Ausín *et al.* [29] reported the spatiotemporal pattern formation of rotating sphere flows from a dynamical system perspective up to $\Omega \leqslant 4$. They observed that the flow field for low Ω yields an analogous transition to the flow past the static sphere with rapid flow frequency variations about the rotation. Interestingly, the transition from a single helix pattern to a double helix structure reveals various regions with hysteric behavior within the wake.

Although there have been many studies on the uniform flow past a transversely rotating sphere at various ranges of Re, studies beyond $\Omega \geqslant 4$ remain absent. On the other hand, how the wake instability would change when the sphere rotates along the streamwise direction is not clearly understood. Therefore, in the present research, we have attempted to address typical wake instability characteristics when the sphere rotates along the streamwise and transverse directions. The dimensionless rotation rates along streamwise and transverse directions are considered between 0.5 and 5. Results for a stationary sphere have also been compared with the rotating case. We have organized the paper as follows: In Sec. II A physical system is briefed, and the mathematical modeling aspects are detailed in Sec. II B, whereas Sec. II C presents numerical methods used. The results section starts with the vortex topology in Sec. III A, where the penetration of the sphere's streamwise rotation through the downstream vortex structures is analyzed. The wake instabilities during the rotation cycle are characterized in Sec. III B. Next, the vortex trajectories are shown in Sec. III C to reveal how the local rotation causes the movement of vortex centers. The insights during the streamwise rotation of the sphere are discussed in Sec. III D, whereas the corresponding analysis for transverse rotation is detailed in Sec. III E. Finally, the paper concludes by drawing the key findings of the research in Sec. IV.

II. PHYSICAL SYSTEM AND MATHEMATICAL SETUP

A. Physical system

Figure 1 represents a schematic of the physical problem involving a uniform left-to-right free stream flow (U_∞) past a rotating sphere. The Cartesian coordinate system is aligned with the sphere's center, where the x, y, and z axes designate the streamwise, cross-stream, and transverse directions, respectively. The rotation axis of the sphere for streamwise rotation is about the x axis, while for transverse rotation it is about the z axis. We define the dimensionless rotational speed as a measure of the ratio between the linear velocity of the sphere to the free-stream speed, $\Omega = \alpha D / 2U_\infty$. Here α and D are the angular velocity and diameter of the sphere. The Reynolds number based on the sphere's diameter is expressed as Re = $U_\infty D / \nu$, where ν is the kinematic viscosity of the fluid. At a representative Re = 500 [24], we have chosen the cases for low to high rotational speeds of the sphere. Accordingly, in the present research, we have considered three streamwise and transverse speeds, namely $\Omega_x = 0.5, 2, 5$ and $\Omega_z = 0.5, 2, 5$. Besides, the corresponding situation for a stationary sphere $\Omega = 0$ is also compared in our analysis.

B. Mathematical setup

The constant property incompressible mass and momentum conservation equations constitute the governing equations for the flow around the sphere. We have used D as the length scale, U_∞ as
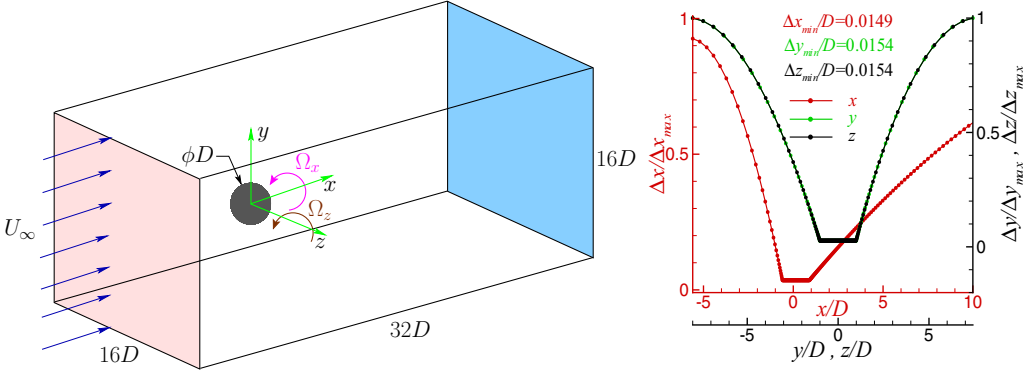
FIG. 1. Schematic diagram showing uniform flow past a sphere. The sphere is constrained to rotate in the streamwise (Ω_x) and transverse directions (Ω_z). The right side panel shows distribution of spatial grid resolution normalized by maximum mesh sizes (Δx, Δy, $\Delta z)_{\mathrm{max}}$ along the x, y, and z directions.

the velocity scale, and D/U_∞ as the timescale for reducing the governing equations dimensionless. The resulting dimensionless form of the governing equations may be expressed as

$$\frac{\partial u_i}{\partial x_i} = 0, \tag{1}$$

$$\frac{\partial u_i}{\partial t} + \frac{\partial (u_i u_j)}{\partial x_j} = -\frac{\partial p}{\partial x_i} + \frac{1}{\mathrm{Re}} \frac{\partial^2 u_i}{\partial x_j \partial x_j}. \tag{2}$$

Here x_i and u_i are the dimensionless coordinate axes and velocity, respectively.

We have chosen the domain extents $32D$, $16D$, and $16D$ in the streamwise, transverse, and cross-stream directions. At the inlet a uniform velocity $(u, v, w) = (1, 0, 0)$ boundary condition is specified. In the exit plane, a convective boundary condition $\partial u_i / \partial x = 0$ is imposed to minimize the upstream feedback and easy passage of the vortices. Boundary conditions in the shear-free horizontal boundaries read $\partial (u, w)/\partial y = 0$, $v = 0$, whereas on the vertical side boundaries $\partial (u, v)/\partial z = 0$, $w = 0$. The boundary conditions on the sphere surface are no slip and no penetration. At all boundaries, we have imposed zero normal pressure gradients except for the exit plane, where the ambient pressure is prescribed at $p = 0$. In our research, we have started all the cases from a no-flow state and let them settle to a dynamic steady state stage. The time average fields shown in our analysis are obtained by considering approximately 30 shedding cycles after the dynamic steady state. The drag, lift, and spanwise force coefficients are defined as $C_{x,y,z} = F_{x,y,z}/(\frac{1}{2}\rho U_\infty^2 D^2)$, where F_x, F_y, and F_z are the components of drag, lift, and spanwise forces acting on the sphere.

C. Numerical setup

The conservation equations are solved using a nonstaggered finite volume technique. We have used the diffuse interface immersed boundary method [33–35] to resolve the complex boundaries. For more details, please refer to De and Sarkar [36,37]. We have employed a nonuniform Cartesian mesh with uniform grids enveloping the sphere at all times for transient computations. The grid spacing distributions in all coordinate directions are shown in the right-hand panel of Fig. 1. We have used a dimensionless time-step size of $\Delta t = 10^{-3}$ for simulating all the cases investigated, which yields a maximum Courant number $\mathrm{Cu}_{\mathrm{max}} = 0.12$ for $\Omega_x = 2$. The total simulation time for all runs has been nearly $20\,000$ core hours on a 850-tFLOP SMP cluster.

We have carried out a mesh sensitivity test at $\Omega_x = 2$ for four progressively refined meshes starting from $M_1 = 168 \times 122 \times 122$ with 25% increments in each extent while keeping the time-step value as $\Delta t = 10^{-3}$. The results of the mesh sensitivity test are obtained in terms of

TABLE I. Mesh sensitivity test results for four progressively refined meshes M_1, M_2, M_3, and M_4 at $\Omega_x = 2$. Here C_x' and C_y' are the rms of drag and lift coefficients. N_x, N_y, and N_z are grids in the x, y, and z directions, respectively.

Mesh	$N_x \times N_y \times N_z$	C_x'	C_y'
M_1	$168 \times 122 \times 122$	2.787×10^{-2}	2.912×10^{-2}
M_2	$216 \times 152 \times 152$	3.152×10^{-2}	3.125×10^{-2}
M_3	$272 \times 190 \times 190$	3.865×10^{-2}	3.662×10^{-2}
M_4	$330 \times 240 \times 240$	3.868×10^{-2}	3.662×10^{-2}

the rms force coefficients and are tabulated in Table I. As seen in the table that for increasing mesh resolution beyond M_3, there is not much difference between the results. Therefore, it may be safely concluded that M_3 mesh is adequate for obtaining grid-insensitive results. However, to obtain a better wake resolution in the subsequent computations, we have chosen the finest mesh size $M_4 = 330 \times 240 \times 240$ as the grid-independent mesh. We have performed 3D computations for the flow past a stationary sphere for Re $\leqslant$ 300 and compared our results with the experimental and numerical data reported in the literature [30–32]. In Fig. 2(a), we have shown the comparison results on the variations of drag coefficient (C_x) as a function of Re. Figure 2(b) compares the functional dependence of separation length X_s with Re, whereas in Fig. 2(c) we show the comparison results for the time evolution of C_x at Re = 300. Given the uncertainties during experiments and the difference in the solution method, we notice that the agreement is acceptable to excellent.

III. RESULTS AND DISCUSSIONS

We have conducted direct numerical simulations at Re = 500 to assess the implications of three-dimensional flow attributes past a sphere subjected to streamwise and transverse rotations. We demonstrate the results for representative situations of low to high rotation rates and analyze the consequent wake instability characteristics. In particular, the results for a stationary sphere are also shown and compared with the rotational cases.

A. Vortex topology

Figure 3 shows 3D vortex structures visualized with the isosurfaces of Q criteria [38] (at 10% of the global maximum). As shown in the figure, compared with the stationary sphere case, the planar symmetry of the flow is lost, and the vortical structures are significantly altered owing to the sphere's rotation. We see that the sphere's rotation along the streamwise direction causes the
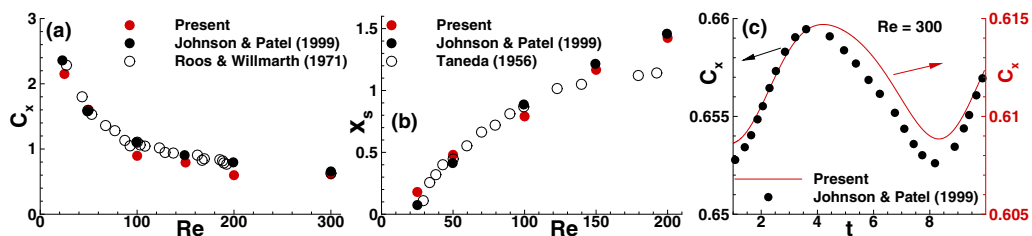

FIG. 2. Comparison of the present simulation results with the (a) experimental and numerical results of Roos and Willmarth [30] and Johnson and Patel [31] for the variations of drag coefficient (C_x) as a function of Re, (b) experimental and computational results of Taneda [32] and Johnson and Patel [31] on the dependence of separation length X_s with Re, and (c) results of Johnson and Patel [31] for the temporal evolution of C_x in an one period at Re = 300.
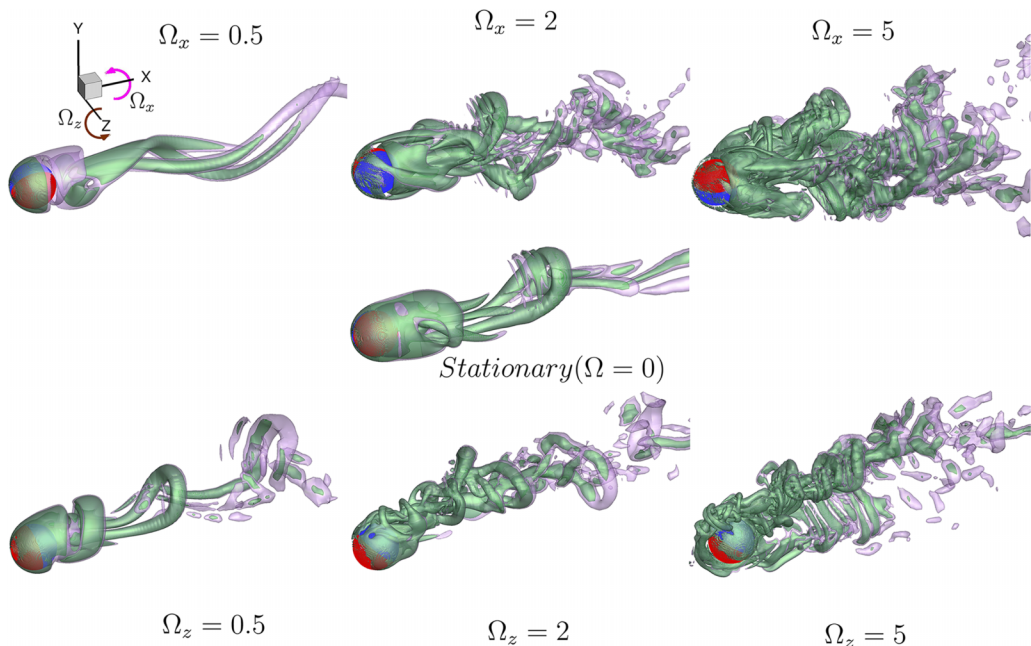
FIG. 3. Three-dimensional vortex structures are visualized by the instantaneous isosurface of Q criteria at 10% of the global maximum for various streamwise and transverse rotation rates. The result for a stationary sphere is shown for comparison. Note that all the vortical structures are shown at the same dimensionless instant.

twisting of the entire vortex structure, leading to centrifugal instabilities. At a low rotation rate of $\Omega_x = 0.5$, in a way, it results in the generation of two intertwined spiral vortices traversing several sphere diameters in the downstream wake [39]. At $\Omega_x = 2$, the streamwise vortex shed from the downstream end of the sphere wraps around with the threadlike structures generated upstream of the sphere surface. The structures then undergo partial coalescence with the primary vortex strand and are bifurcated into multiple vortex filaments. In the downstream wake, the vortex filaments further interact with the threads under it, generating smaller structures that break down into smaller filaments in the far stream. At $\Omega_x = 5$, the streamwise vortices at the downstream end bifurcate into large-scale shear-layer structures with a trigger in their strength. The structures undergo rapid reconnections and break down into smaller vortex filaments in the downstream wake.

The shedding pattern for the transverse rotation of the sphere is subjected to turning, leading to wake deflection. The vortex structure at the opposing side of the rotation is susceptible to squeeze. In contrast, the structures at the aiding side experience tearing. The relative dominance between these two mechanisms yields the formation of dual vortical threads in the near wake by peeling the shear layer from the sphere surface at $\Omega_z = 0.5$. Further downstream, these threads tilt and join in evolving a single-sided shedding of the hairpin structure, as found for a stationary sphere. However, increasing Ω_z triggers tearing over the squeezing of the vortex structures. The structure deforms and breaks into multiple smaller-scale vortex filaments in the near wake. We observe a strong asymmetric wake for $\Omega_z \geqslant 2$, which deflects upward to render a one-sided vortex street. The higher rotation of the sphere induces near-wake instability that breaks the shed vortex into thread dipoles [40]. The threads bend toward the direction opposite the fluid motion (advancing side) and encounter multiple reconnections, forming small-scale vortex filaments in the far stream. That again wraps around the stretched threads, causing weakening of the threads followed by finer scale decay of vortex structures through cross-diffusion. At $\Omega_z = 5$, the vortex structure deflection increases
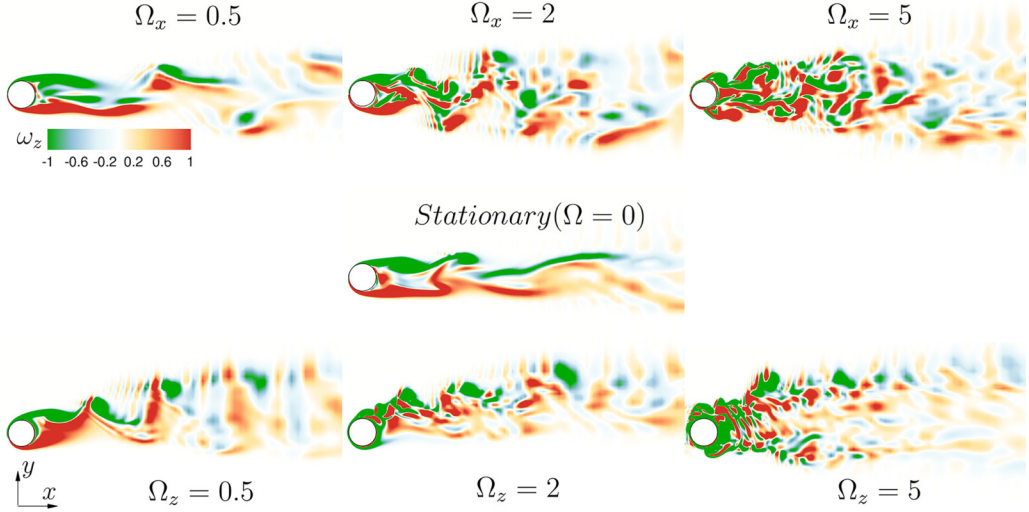
FIG. 4. Instantaneous vorticity contours (ω_z) at $z = 0$ plane for different streamwise and transverse rotation rates. The corresponding contour for a stationary sphere is also shown.

toward the sphere's advancing side, drawing the flow upwards, resulting in a large-scale shedding pattern [41]. The near wake vortex street bifurcates transversely, and the topology shows complex structures consisting of strongly attached stretched hairpins where the legs are entangled with the locally evolving threads.

Figure 4 shows the instantaneous contours of ω_z at $z = 0$ plane. The plot for a stationary sphere shows elongated strands of positive and negative shear layers from the sphere's surface to the far stream. A finger of positive vorticity bends upwards and pushes the negative vortices further up. In contrast, the wake structure at $\Omega_x = 0.5$ shows elongated positive and negative vortex strands from the sphere surface to the far wake. At $\Omega_x = 2$, pair of opposite signed shear layers are intertwined by the sphere's rotation in the back stagnation region. The wake bifurcates into alternatively signed cross-stream cells, developing a zigzag pattern. In the far stream, lateral diffusion of the cross-stream cells renders a blurred wake. Higher rotation at $\Omega_x = 5$ causes thinning of the shear layer, which rolls up close to the sphere's surface and unevenly discharges patches of positive and negative vorticity cells of triggered strength downstream. The downstream circulation cells experience localized stretching and develop irregularly distributed, continuously interacting, complex vortex loops and contrails. The far stream vortex contrails undergo core diffusion due to viscous decay, yielding a blurred wake pattern. At $\Omega_z = 0.5$, the shear layer on the retreating side is deflected toward the advancing side and then interacts with the negative shear layer to form branches of hairpin legs. At $\Omega_z = 2$, shear layers from the retreating and advancing sides merge in the near wake by experiencing local instability, similar to the shear layer instability regime [21,22,24]. Azimuthal stretching splits the wake, generating multiple positive and negative vorticity cells downstream. The shear layers become unstable at $\Omega_z = 5$, causing upstream shedding of vortices (Fig. 4). In the near wake, both the positive and negative vortices roll up and bifurcate into a twin jet-type flow pattern, resulting in the transverse expansion of the wake.

We compute the absolute magnitude of time-averaged vorticity at a streamwise plane,

$$\langle \omega \rangle(x) = \int_{A_{yz}} (\langle \omega_x \rangle^2 + \langle \omega_y \rangle^2 + \langle \omega_z \rangle^2)^{1/2} \, dA_{yz}. \tag{3}$$

Here $\langle \cdots \rangle$ refers to the time average. The streamwise variation of $\langle \omega \rangle$ for a stationary sphere and both rotation rates are plotted in Figs. 5(a) and 5(b), where the shaded region marks the sphere's
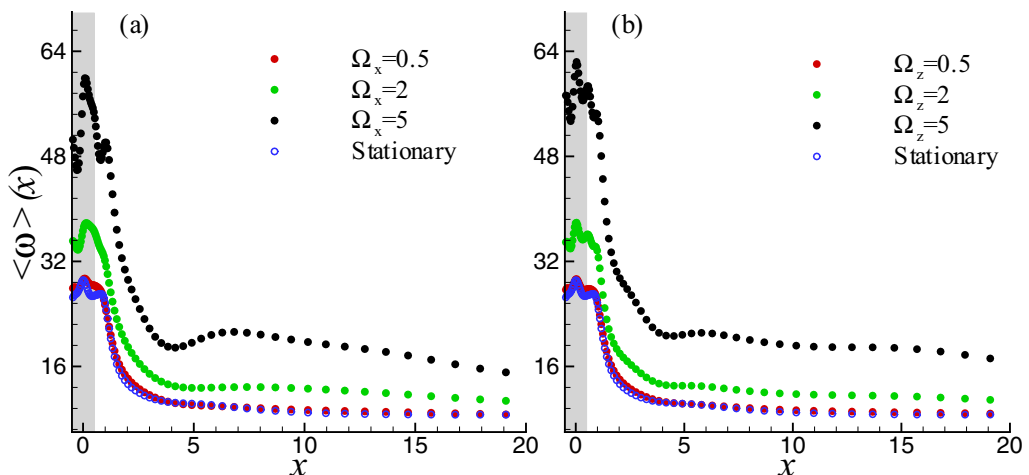
FIG. 5. Streamwise variations of the absolute magnitude of time-averaged vorticity $\langle \omega \rangle$ for a stationary sphere and for various (a) Ω_x and (b) Ω_z. A shaded region shows the sphere's location.

location. The data for a stationary sphere nearly collapse with those for Ω_x, $\Omega_z = 0.5$, which typically signifies the decay of vortex structures from the sphere to the far wake. The distribution of $\langle \omega \rangle$ shows how deep Ω_x and Ω_z effect penetrate in the x direction. We see that $\langle \omega \rangle$ peaks over the sphere surface and decays monotonically with increasing x. Consequently, the structures are in coherence with the forced rotation with the formations of localized circulation cells at various streamwise locations. The local rotation rate increases with the sphere's rotation. The vorticity accumulation is identical for Ω_x and Ω_z. We observe that the sphere rotation induces the strongest wake rotation in its own plane. Only the high rotation rates of the sphere modify the wake nature with a significant rotation component. The shed vortices experience maximum forced-rotation induced circulation for both Ω_x, $\Omega_z = 5$, which eventually penetrate through the large far stream region. In contrast, sphere rotation hardly affects the localized circulation cells beyond $x \geqslant 10$ for Ω_x, $\Omega_z \leqslant 2$. Notably, at Ω_x, $\Omega_z = 5$, there is a local minimum of the $\langle \omega \rangle$ distribution around $x \approx 4$, which is due to the change in shedding regime (more prominent at $\Omega_x = 5$). The distortion, including partial tearing of the primary vortex structure to bifurcate into a twin jet-type flow pattern, renders a loss of the identity of the primary vortices. It is important to note that although there have been dissimilarities between the shed structures, the magnitudes of $\langle \omega \rangle$ for both the rotation rates are similar. Therefore, revealing the global nature of circulation characteristics at various axial planes.

B. Rotation cycle

Figure 6 presents temporal evolution of vortical structures for the instances (a–h) in a complete rotation cycle at $\Omega_x = 0.5$, where the corresponding plots for $\Omega_x = 2$ is shown in Fig. 7. We have demonstrated the vortex structures by the isosurfaces of Q at 10% of the global maximum. The drag (C_D) and lift (C_L) signals are portrayed in the insets. The vortex structures shown in $a \rightarrow h$ equal one dimensionless rotational period, $\tau = 2\pi/(\alpha D/U_\infty) = 2\pi/2\Omega = \pi/\Omega$. In contrast, the period of C_D, C_L are different from that of τ, and its variation is shown here within the dimensionless period τ. The vortex structures show a pair of steady vortex threads attached to the sphere surface in the near wake at $\Omega_x = 0.5$. The flow is steady, and no vortex shedding is observed. The vorticity diffusion gets affected by the close velocity contours due to the surface-driven boundary layer around the sphere [24], yielding the ceasing of the vortex shedding. The threads in the far wake wrap around due to the relative angular rotation in the streamwise direction, and as a result, we observe spiral formation in the downstream wake. The small footprint of the wake leads to less form drag, resulting
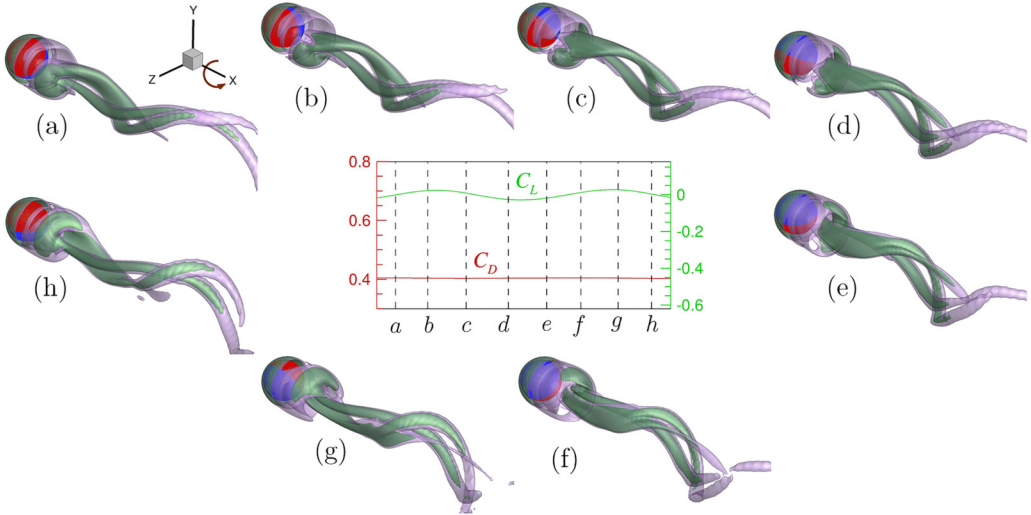
FIG. 6. Rotation cycle visualized by the three-dimensional vortex structures by the instantaneous isosurface of Q criteria at 10% of the global maximum for $\Omega_x = 0.5$. The inset shows the temporal evolutions of C_D and C_L. The vortex structures shown in $a \to h$ equal one dimensionless rotational period, $\tau = 2\pi/(\alpha D/U_\infty) = 2\pi/2\Omega = \pi/\Omega$. Note that the period of C_D and C_L are different from that of τ.

in a lower fluid volume in the near wake. This is reflected in the drag and lift signals, where we notice a constant C_D magnitude for the entire rotation cycle. In contrast, C_L shows trivial fluctuations in the neighbourhood of $C_L \approx 0$.

At $\Omega_x = 2$, we observe vortex shedding with the periodic formation of hairpin-type structures in the downstream wake. It is found that the separation point moves upstream along the direction
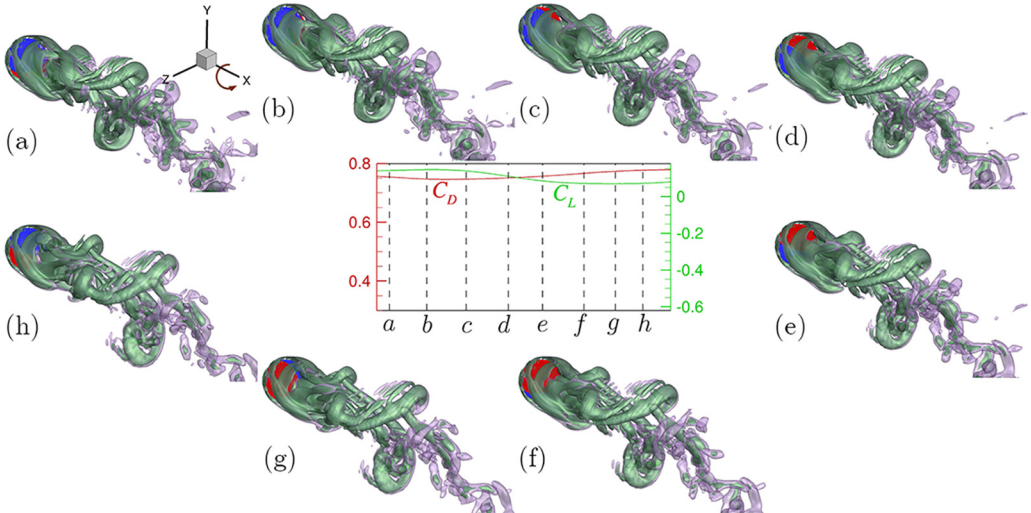

FIG. 7. Three-dimensional visualization of the rotation cycle with vortex structures by the instantaneous isosurface of Q criteria at 10% of the global maximum for $\Omega_x = 2$. Time variations of C_D and C_L are shown in inset. As depicted in $a \to h$, the wake structures correspond to one dimensionless rotational period $\tau = \pi/\Omega$. The period of C_D and C_L in the insets are different from that of τ.
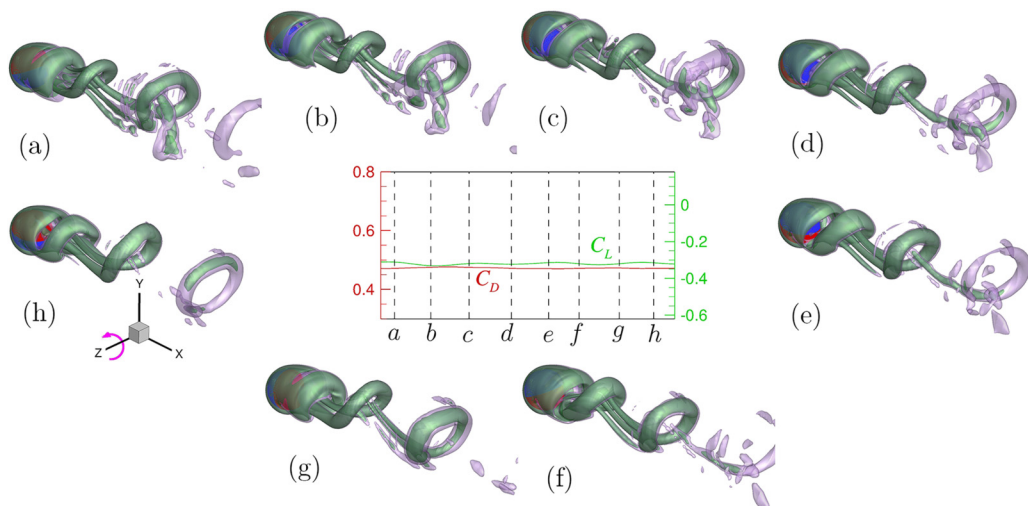
FIG. 8. The instantaneous Q isosurfaces of the three-dimensional vortex structures at 10% of the global maximum in a complete rotation cycle for $\Omega_z = 0.5$. The inset shows the time variations of C_D and C_L. Here the vortex structures, shown in $a \rightarrow h$, correspond to one dimensionless rotational period $\tau = \pi/\Omega$, while the periods of C_D and C_L are different from that of τ.

of the sphere rotation. The high streamwise rotation of the sphere causes stretching of the shear layers at the sphere's surface. The stretched shear layers from either side of the sphere undergo higher generations of reconnection, forming a series of hairpin vortices shedding bidirectionally in the downstream wake. The resultant wake appears to be a blunt shape, and no particular vortex shedding pattern is seen. As evident, the blunt wake hardly rotates during the consecutive instances of the rotation cycle (a–h). This out-of-sync motion of the shed structures with the sphere's rotation contributes to a larger magnitude of drag generation, as evident from the inset. The shed structures constituting the wake experience higher rotational inertia, which is generally reflected by the topologically alike wake structures for the instances (a–h). We also note that the lift magnitude is small and $\Delta C_L \approx 0$.

We present in Fig. 8 the isosurfaces of Q (at 10% of the global maximum) for $\Omega_z = 0.5$ at the instances (a–h) in a complete rotation cycle, whereas Fig. 9 depicts the corresponding results for $\Omega_z = 2$. In stark contrast to the situation at $\Omega_x = 0.5$, we observe one-sided vortex shedding when the sphere undergoes turning motion at $\Omega_z = 0.5$. The rotation sequence begins with the roll-up of the shear layer on the lee side of the sphere. Roll-up layers grow in size in the successive instants by accumulating peeled-up shear layers separating from the advancing side of the sphere's surface. In the later stage, the rolled-up layers evolve into a hairpin vortex structure convecting downstream after detaching from its source. As the hairpin propagates, they develop and become more diffused, although they retain their shape as Ω_z is low. Legs of the hairpin approach each other via curvature-induced self-induction and merge to form ring-tail-like structures downstream. The tail, having lower strength, experience rapid diffuson in the far stream, and we observe the shedding of a ringlike vortex structure. Notably, there is a one-ring formation per cycle. The lift and drag signals are nearly uniform during the period a–h, although C_L is always negative.

For the higher rotation rate at $\Omega_z = 2$, the separation point advances upstream, and we observe that the vortex structures experience high-intensity core instability. As a result, the vortex loops start to roll up randomly from the advancing side of the sphere and in different directions. The turning motion causes the wake to deflect upward, forming a top-heavy shear layer. The resulting consequence is reflected in $C_L < 0$ for the entire rotation sequence. The vortex structures wrap around each other, and we do not discern any specific shape of the wake vortices. We found that
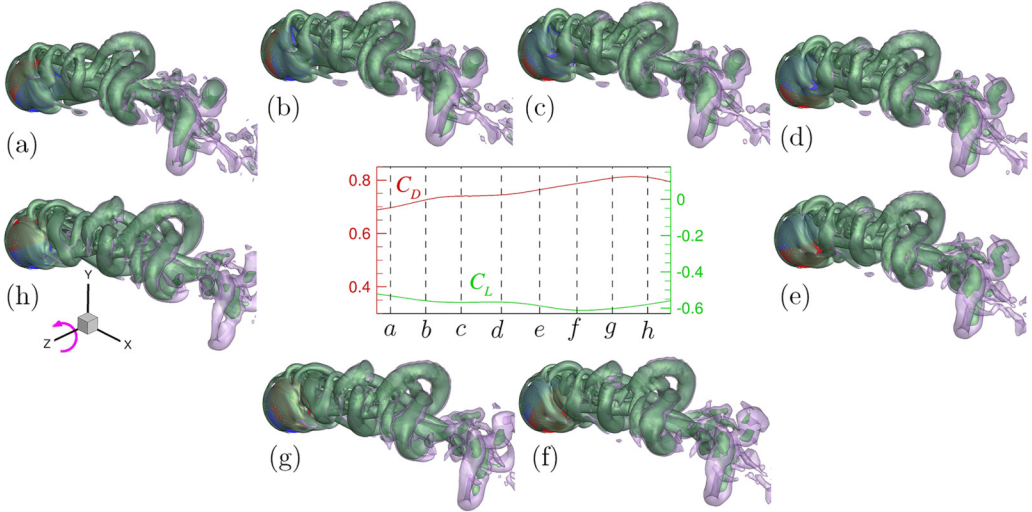
FIG. 9. Isosurfaces of three-dimensional vortex structures visulaized by the Q criteria at 10% of the global maximum in a complete rotation cycle for $\Omega_z = 2$. Evolutions of C_D and C_L are shown in the inset. Note that the evolutions of vortex structures shown in $a \rightarrow h$ correspond to one dimensionless rotational period $\tau = \pi/\Omega$. In contrast, the period of force signals, C_D, C_L in the insets, are different from that of τ.

the wake cannot cope with the high sphere rotation. As a result, the structures retain their shape and orientation during the successive instances of the rotation cycle. The structures undergo core diffusion in the far stream to yield randomly oriented vorticity patches.

To gain more insights into the wake dynamics, in Fig. 10, we show the line-time reconstruction of v along the streamwise direction at a vertical section $y = d/2$ on $z = 0$ for 10 shedding cycles. At a given x, if we draw a vertical line, then it shows how the wake evolves with time. We observe that for $\Omega_{x,z} = 0.5$, the line intersects the wake at negative and positive values alternatively, which clearly marks the highly periodic and coherent vortex structures across the streamwise extent. The flapping of the shear layers is significant for lower $\Omega_{x,z}$. However, the change in the sign of v is
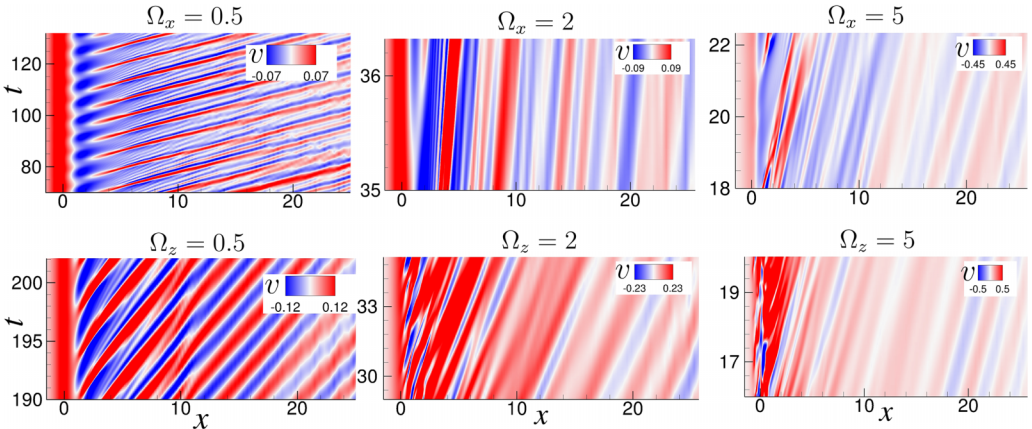

FIG. 10. Line-time reconstruction of the vertical velocity (v) along the streamwise direction at a vertical section $y = d/2$ on the midspan plane $z = 0$. Here, the time evolution is shown along the y direction while the x axis denotes the streamwise direction.

trivial for larger rotational speeds. As a result, the flapping motion cannot penetrate downstream. Hence, the wake instabilities are limited in the near wake. For $\Omega_z = 0.5$, we observe the broadening of both positive and negative cells, which reveals the growth of large-scale deformation associated with the flattening of the vortex core. Between the shed vortices, a constant time lag is observed for $\Omega_x = 0.5$ and is higher for $\Omega_z = 0.5$. The periodicity of the shed structure is lost for higher $\Omega_{x,z}$. We observe intermitted bands of positive and negative cells undergoing streamwise diffusion, which is attributed to the far wake fragmentation of the threads into filaments. The discontinuity in vortex formation is evident for higher Ω_x and Ω_z, which is a result of severe relative velocity between the sphere and the near wake. In contrast, for a specified t, we witness the same signed v velocity occupying a larger downstream section at a higher $\Omega_{x,z}$. This indicates that the vortex breakdown occurs early, culminating in the gradual convection of the well-mixed fluid downstream.

C. Vortex trajectory

We track instantaneous vortex trajectories at various transverse (*y-z*) planes to examine how the local rotations cause the movement of vortex centers. Here we extend the experimental vortex center identification algorithm proposed by Graftieaux *et al.* [42] for the present 3D problem. For flow through a circular path, we consider some point "S" and any point "R" inside and on the circle. We define a function ζ_S as

$$\zeta_S = \frac{1}{A_\alpha} \int_{A_\alpha} \left| \frac{\overline{SR} \times \overline{V}}{|\overline{SR}||\overline{V}|} \right| dA. \tag{4}$$

Here $\overline{V}$ is the velocity vector, A_α is the local neighborhood of "S," and $|\cdots|$ is the magnitude. Therefore, as one approaches the center of a circle, $\zeta_S \to 1$. We adopt this method for tracking the instantaneous vortex centers. We compute ζ_S for all domain points, assuming a small neighborhood A_α around it. As a result, we obtain multiple close-by points satisfying $\zeta_S \approx 1$. Hence, we choose a global maximum of ζ_S to avoid duplicacy in identifications. Therefore, vortex trajectories are plotted as the locus of the vortex centers where ζ_S attains a global maximum within spatial region A_α.

The vortex trajectories at various transverse planes are shown for different streamwise and transverse rotation rates in Figs. 11 and 12, respectively. The direction of rotation of the vortex trajectories during streamwise rotation is shown in blue arrows. The transverse rotation direction of the trajectories in a *y-z* plane is out of the plane and hence not shown in Fig. 12. The vortex trajectories clearly show the radial motion of the localized vortices at various *y-z* planes in sync or out of sync with the sphere's rotation. For $\Omega_x = 0.5$, the trajectories at all streamwise stations are in sync with the sphere's motion, indicating the wake rotation following the sphere. As a result, the trajectories move in a circular path in the near wake, whereas the far wake trajectories settle at a larger radius. The maximum diameter of the trajectory orbit reaches an approximately constant value of twice the sphere's diameter. Notably, the vortex core at all planes always occupies the sphere's footprint (shown by a solid circle), marked by the congregation of vortex centers.

The figure shows that a higher rotation rate at $\Omega_x = 2$ significantly affects planer vortex trajectories. In the near wake $x \leqslant 4$, the vortical structures past the sphere try to rotate in the same direction as the sphere's rotation. However, owing to the higher angular velocity of the sphere, the local rotation center cannot cope with high Ω_x. As a result, we observe scattered centers of the vortex motion paths that eventually lead to a larger wake footprint. We found that the fluid particles at such a larger rotational speed partially obey the consequences of solid-body rotation. At each plane, a higher sphere rotation triggers the angular velocity of the revolution of each fluid particle about the center. Accordingly, fluid particles try to retain their location relative to other particles. In turn, there is a preferential distribution of the vortex centers along a radial line from the sphere, where the vortex trajectories follow along the radial paths from the center. Therefore, with increasing radial distance (*r*) from the center, the angular velocity triggers liner velocity (u_θ) of the fluid particles across the radial line. Since, for a solid-body type motion, $u_\theta = \Omega_x r$. Therefore, closer to the wake
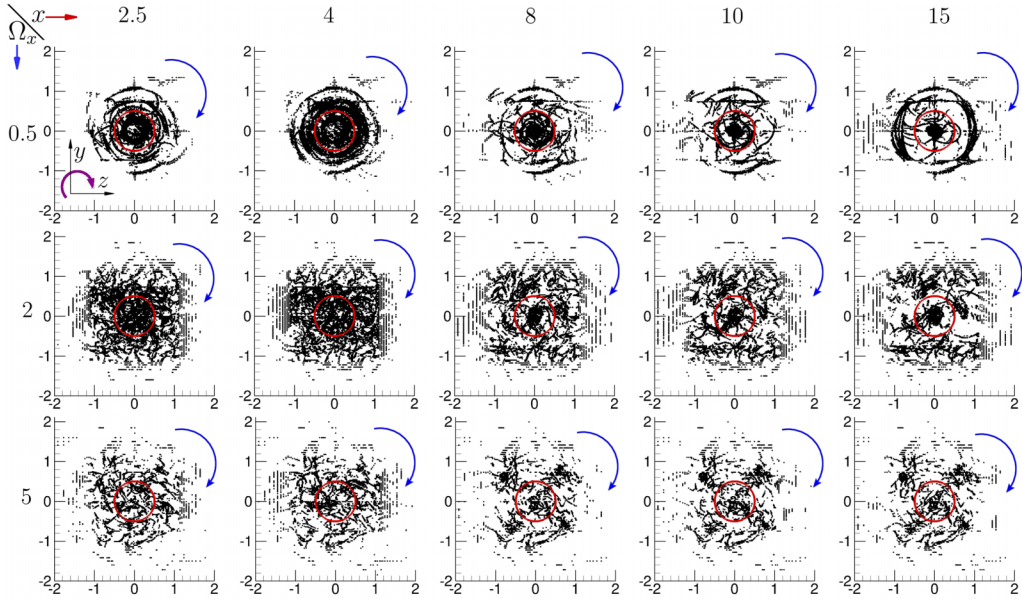
FIG. 11. Streamwise variations of the vortex trajectories at different transverse (*y-z*) planes for various streamwise rotation rates. The direction of rotation of the vortex trajectories is shown in blue arrows, whereas the location of the sphere about each plane is shown as a solid circle.

boundaries, the fluid particles move faster than the particles preceding them. The overall effect is shown by a curved vortex trajectories across the *y-z* planes. On the contrary, the rotational speed of the vortical structures in the far wake decreases with increasing downstream distance from the sphere. We found that the trajectories move apart azimuthally. The result is lesser mixing of the fluid across these planes.

At $\Omega_x = 5$, we see that higher degrees of mixing of the fluid particles in the near wake reduce localized rotation of the vortex trajectories. However, the far wake shows the vortex centers settle along the radial lines. The vortex trajectories bear the consequences of rigid-body type motion at different transverse planes for this rotational speed. Near the wake boundaries, the trajectories follow a curved path, whereas the motion is almost through a radial line closer to the center. We observe that the trajectories settle along four lines rotating about the center. Notably, the wake rotation experiences phase lag with the sphere. As a result, the vortex centers approach the wake boundary without deformation because the viscous stresses are minimal in this flow. We notice that vortex centers populate less around the sphere's footprint than $\Omega_x = 2$.

The vortex trajectories show symmetric distribution at all transverse planes for $\Omega_z = 0.5$. We see that the flow is induced along the axis of rotation, causing the vortex centers to move toward the negative *z* axis. We attribute this observation to the one-sided shedding of hairpin vortices. We see from Fig. 8 that the turning motion of the sphere causes the structures to tilt slightly along the axis of rotation during vortex shedding. The vortex trajectories are spread vertically about the rotation axis, with the core encompassing the maximum concentration of vortex centers. They are primarily counter-rotating pairs of streamwise legs of the hairpins where the tip confines the core. The legs grow in size downstream, causing the vortex centers to cover a wide area. However, the far stream diffusion yields thinning of hairpin structures. That eventually leads to a reduction in vortex centers population noticed in the far wake.

The induction of trajectories toward negative *z* axis continues to exist at $\Omega_z = 2$, which is again due to the one-sided vortex shedding shown in Fig. 9. The vortex centers are more scattered across the transverse planes. Although in the near wake, trajectories are clustered along the rotation
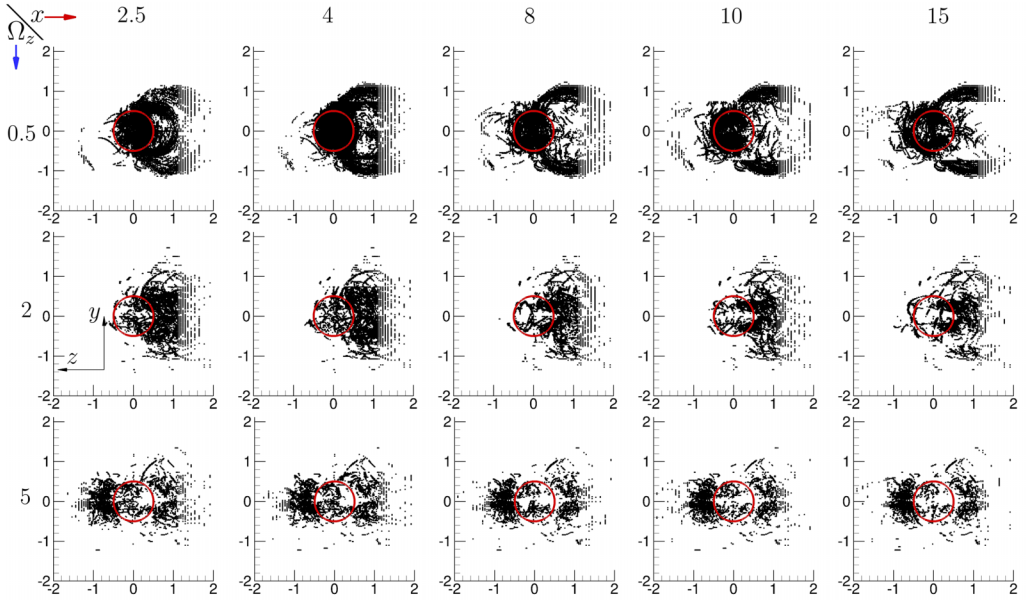
FIG. 12. Vortex trajectories at different transverse (y-z) planes for various transverse rotation rates. The location of the sphere about each plane is shown as the solid circle.

axis. We observe that the trajectories appear symmetric about the $z = 0$ axis. This is owing to the structural similarity of the vortex structures during consecutive instances of the rotation cycle. As a result, the vortex centers at various streamwise planes almost retain its position and orientation during the vortex shedding.

With increasing transverse rotation, we have seen that the separation points approach upstream of the sphere's surface. Notably, at $\Omega_z = 5$, shedding of vortices starts from the front stagnation zone of the sphere. Besides, the roll-up vortex structure bifurcates into twin-jet type shedding patterns in the near wake (Fig. 3). Such a consequence is reflected in the vortex trajectories, where we observe that vortex centers are symmetrically distributed in the $\pm z$ axis. It is found that the vortex centers do not spread vertically. Instead, they follow a horizontal motion. However, Fig. 12 shows the less rotational effect on the footprint of the sphere.

We report the dynamic behavior for the drag, lift, and transverse force coefficients acting on the sphere by plotting phase portraits of (C_z, C_y) and (C_x, C_y) in Figs. 13 and 14, respectively. The corresponding phase diagram for a stationary sphere is also shown for comparison. We observe
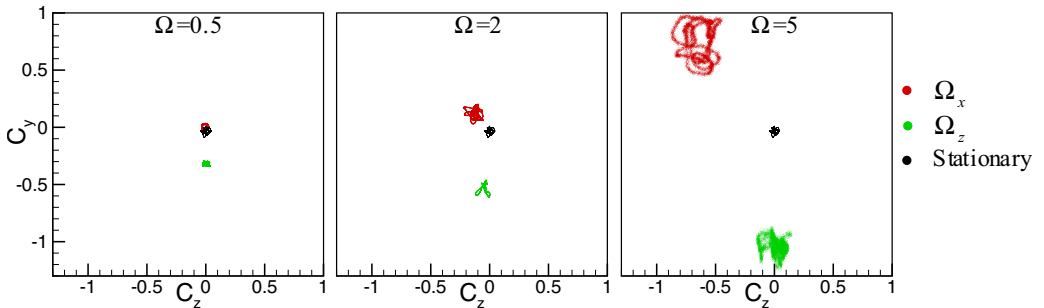

FIG. 13. Phase diagrams of C_y and C_z for various streamwise and transverse rotation rates.
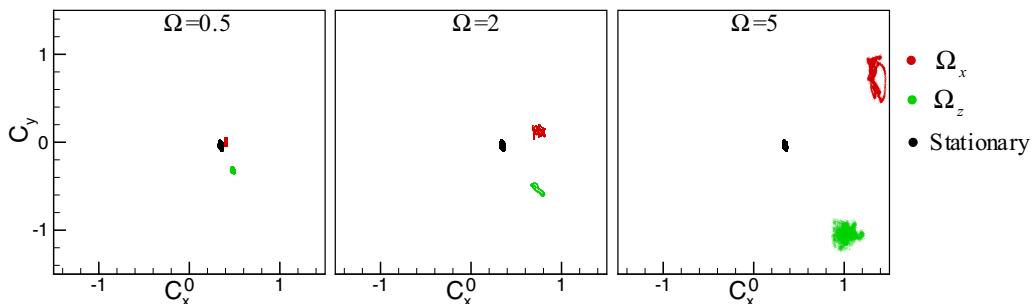
FIG. 14. Phase portraits of C_y and C_x for various streamwise and transverse rotation rates.

that, in general, the phase plots change irregularly and have a preferential orientation toward both positive and negative C_y axis. It is found from Fig. 13 that the phase diagram falls on a point for a stationary sphere. However, the sphere experiences a positive lift for increasing Ω_x. At $\Omega_x = 0.5$, the sphere behaves like a stationary sphere with negligible C_y and C_z. Nevertheless, the sphere encounters negative C_z for increasing Ω_x. In contrast, a transversely rotating sphere always induces a negative lift owing to the flow induced in the negative y direction due to the "Robins-Magnus" effect, as shown in the figure. As a result, C_y is negative at $\Omega_z = 0.5$ and becomes more negative for increasing Ω_z. However, C_z is almost zero for all cases, except at $\Omega_z = 5$, where we notice a small variation along the $\pm C_z$ axis. We attribute this to the upstream shedding of vortices followed by a twin-jet type flow bifurcation in the near wake that eventually induces a flow bias through the rotation axis.

Irrespective of the rotation directions, a rotating sphere always experiences a positive drag, as revealed in Fig. 14. The magnitude of drag increases with rotational speed and is independent of the sign and magnitude of lift coefficients that the sphere is subjected to. In particular, we observe a positive drag for the stationary sphere, although the lift is nearly trivial. It is seen that both (C_x, C_y) and (C_z, C_y) show large oscillations at Ω_x, $\Omega_z = 5$. An increase in oscillation magnitudes may be due to an increase in the near wake pressure fluctuations that trigger the generation of complex vortex structures, as observed in Fig. 3.

D. Streamwise rotation

As discussed previously, effect of the sphere's rotation does not penetrate the far wake. In turn, vortex structures at various streamwise stations rotate at speed different from the sphere's rotational motion. We examine such a consequence by computing the angular velocity of the wake vortex, $\Omega_v(y, z)$, at various transverse (y-z) planes located at different streamwise stations. For a streamwise station p, we define the area average angular velocity of the vortices at any y-z plane having an area A_{yz} as

$$\Omega_p(x, t) = \frac{1}{A_{yz}} \int_{A_{yz}} \Omega_v(y, z) \, dA_{yz}. \tag{5}$$

We have calculated the value of Ω_p as follows: For any y-z plane along any streamwise station p, if S is the mean position of the sphere and Q is any point on the plane, then one may compute the radius $r = |\vec{SQ}|$. The azimuthal and angular velocities at the point Q about the mean poisition S may be obtained as $u_\theta = -v \cos\theta + w \sin\theta$ and $\Omega_v(y, z) = u_\theta/r$, respectively. Furthermore, by computing angular velocities for all the points within the plane y-z and on integrating within the planar area A_{yz}, one may obtain the numerical value of Ω_p as shown in the equation above.

Figure 15 shows streamwise variation of the time average normalized angular velocity, $\langle \Omega_s \rangle = \langle \Omega_p(x, t) \rangle / \Omega$, at each streamwise rotation rate. At a given Ω_x, the value of $\langle \Omega_s \rangle$ decays
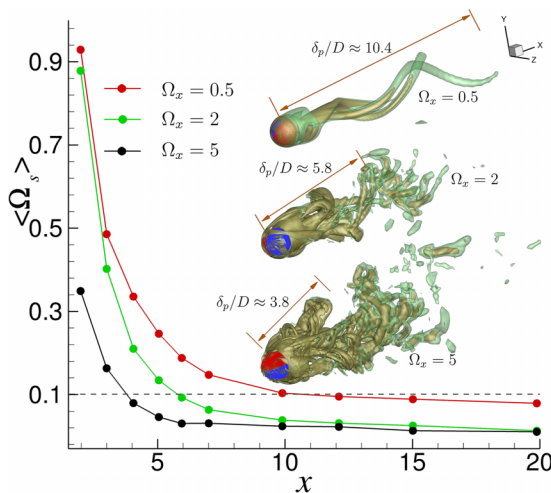
FIG. 15. Streamwise dependence of time average normalized angular velocity at various transverse (y-z) planes for different streamwise rotation rates. Estimated penetration depths for various Ω_x are indicated in the corresponding Q structures.

monotonically from the near wake to far stream saturation. We observe far wake saturation for $\Omega_x = 0.5$. However, it is revealed that $\langle\Omega_s\rangle$ saturates early in the near wake with increasing Ω_x. As can be seen from the figure, the near wake vortices at $x = 2$ could cope up with the sphere's rotation for $\Omega_x = 0.5$, whereas it is reduced marginally for $\Omega_x = 2$. In contrast, much of the rotational speed is lost for $\Omega_x = 5$. Compared to $\Omega_x = 0.5$, the downstream decay of $\langle\Omega_s\rangle$ is much faster for $\Omega_x = 2, 5$, yielding a steeper curve. This result clearly indicates that the penetration of angular velocity of the sphere to the downstream vortices varies with Ω_x. In this context, we define the penetration depth as

$$\langle\Omega_p(x = \delta_p/D, t)\rangle = \beta\Omega. \tag{6}$$

In the present study, we have chosen the threshold parameter $\beta = 0.1$. Thus, δ_p marks the downstream distance for which up to 10% of the sphere's angular speed is preserved by the downstream vortical structures. We have shown the numerical values of δ_p/D in the insets of the figure with lateral measures in the respective instantaneous vortical structures visualized by the Q criteria. The value of δ_p/D is largest at $\Omega_x = 0.5$, where we see that the sphere's rotation influences nearly the entire downstream wake. As a result, the wake tries to rotate with the sphere, causing a gross twisting of the downstream vortices. That, in turn, culminates in intertwined spiral vortices. It is noted that increasing Ω_x causes a rapid reduction of the penetration depth. For $\Omega_x = 2$, the near wake vortices are in sync with the angular velocity of the sphere, and as a result, we observe a clear twisting of the vortical structures to $\delta_p/D \approx 5.8$. However, the wake instability causes the structures to bifurcate into multiple vortex filaments beyond the penetration depth, where the structures cannot preserve the sphere's angular velocity. The penetration depth is minimum at $\Omega_x = 5$, where the flow is inherently unstable, reducing the influence of Ω on the wake vortices. We see the formation of complex vortex structures in the wake with multiple bifurcations into small-scale structures. Thus, the effect of Ω on the wake vortical structures are limited to a region closer to the sphere.

To infer how the dominant azimuthal frequency of $\Omega_p(x, t)$ differ relative to Ω, in Fig. 16 we have shown the dependence of normalized angular frequency of the vortices, f_Ω/f_s, as a function of Ω_x at various streamwise stations. Here f_Ω and f_s are the frequencies of $\Omega_p(x, t)$ and Ω, respectively. We have performed fast Fourier transform of the time signals of $\Omega_p(x, t)$ and obtained the dominant frequency f_Ω. This figure clearly establishes that the vortex structures at different downstream
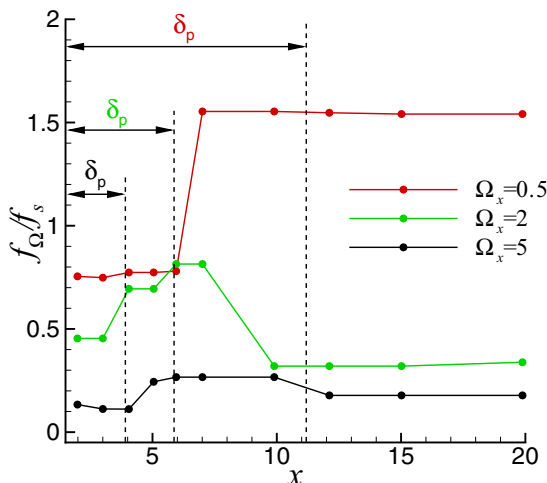
FIG. 16. Plot of the normalized angular frequency of the vortices, f_Ω/f_s, as a function of Ω_x at various streamwise stations.

stations rotate asynchronously with the sphere, $f_\Omega \neq f_s$. In general, with respect to f_s, the angular velocities of the vortices at various downstream stations are at high-frequency levels for $\Omega_x = 0.5$. In contrast, $f_\Omega \neq f_s$ decreases with increasing Ω_x. From this, we may conclude that the entire wake at $\Omega_x = 0.5$ is dominated by high-frequency motion. Nevertheless, we have seen that the vortex structure triggers its strength at higher Ω_x. The normalized angular frequencies of the near wake vortices at $\Omega_x = 0.5$ are nearly equal. The low-frequency rotation in the near wake is asynchronous, signifying torsion of the vortex structures. However, at $x \approx 6$, it shows a discontinuous jump to saturation in the far stream. Analogous behavior is also noticed for other rotational speeds, albeit the saturation of f_Ω/f_s occurs early in the near wake for increasing Ω_x. The jump in f_Ω/f_s is perhaps due to the detachment of the primary vortex strand from the source. We observe a plateau region in the normalized frequency plot for $\Omega_x = 2, 5$, where f_Ω/f_s remains nearly at the same level for the corresponding streamwise stations. We attribute this observation to the zone of wake transition, where the primary vortices bifurcate and form many interconnected vortex loops. The strain rate causes the vortex loops to split into multiple vorticity cells in the far stream (Fig. 3). In this plateau region, where $\langle \Omega_s \rangle$ is higher, the wake breaks down indicating termination of δ_p. Beyond the transition zone, the small-scale structures rotate at a lower frequency, and as a result, we observe a drop in f_Ω/f_s values before far stream saturation. The vortices settle for a smaller $\langle \Omega_s \rangle$. The sphere angular velocity does not reach this region and is primarily dominated by the wake instability.

Figure 17 shows the time histories of normalized angular velocity at three different streamwise stations marked by the corresponding f_Ω/f_s transitions shown in Fig. 16 for different Ω_x. Based on the nature of wake transition and different regions in the frequency plot in 16, we have chosen three representative regions, namely near wake at $x = 3$, transition/plateau region at $x = 6$, and the saturation/far-wake region at $x = 10$, respectively. We observe periodic/quasiperiodic behavior of $\Omega_s(t)$ in the near wake at $x = 3$. As can be seen, $\Omega_s(t)$ shows periodic fluctuations for $\Omega_x = 0.5$ and become quasiperiodic for increasing rotation rates. It is found that the smaller angular velocity of the sphere induces larger $\Omega_s(t)$ with a rapid change in angular acceleration and deceleration. The amplitudes of oscillations reduce from the near to far wake stations. A same trend is also noticed for the transition zone ($x = 6$) and far wake ($x = 10$) locations. The transition region ($x = 6$) shows lower magnitude of $\Omega_s(t)$. There are frequent evolutions in $\Omega_s(t)$ with small timescale changes. The angular velocity of the sphere greatly influences the instantaneous angular velocities of the vortex structures in the near wake at $\Omega_x = 0.5$. In contrast, it is suppressed for $\Omega_x = 2, 5$, and the
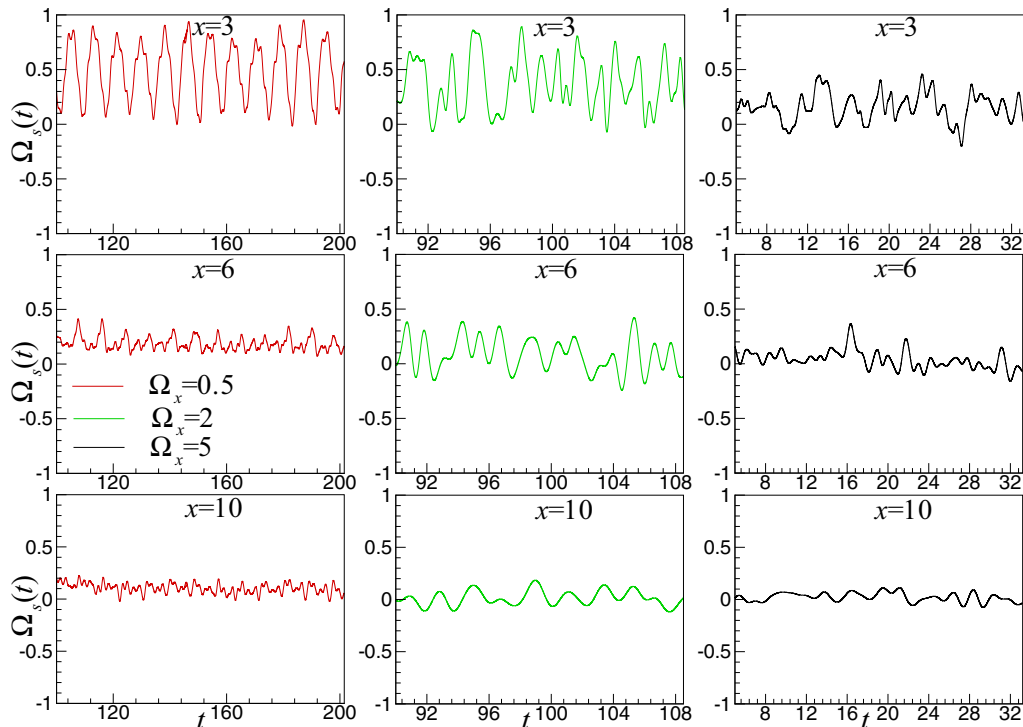
FIG. 17. Time histories of normalized angular velocities with the angular velocity of the sphere at various streamwise locations for different streamwise rotation rates.

structures cannot carry the rotational inertia of the sphere. We observe that $\Omega_s(t)$ is always positive for $\Omega_x = 0.5$. However, it alternatively changes the sign for higher values of Ω_x. Such occurrences are most prominent in both transition and far wake locations for $\Omega_x = 2, 5$. At higher rotation rates, the structures experience bifurcations into small-scale vortex filaments, which undergo localized rotations about their core in the clockwise and counterclockwise directions, respectively. This is not discerned at $\Omega_x = 0.5$, where we oversee a pair of two intertwined spiral vortices covering the entire downstream wake (Fig. 3). Notably, in the saturation region ($x = 10$), there is a trivial change in $\Omega_s(t)$. The effect of the sphere's angular velocity does not reach this zone, and the wake instability mainly dominates the vortex motions.

E. Transverse rotation

We investigate the effect of transverse rotation on the angular velocity at various streamwise locations. In Fig. 18(a), the plot of $\langle \Omega_s \rangle$ with x is shown for different Ω_z. It is found that compared to the streamwise rotation, transverse rotation of the sphere has an insignificant effect on the rotation of the vortices. Therefore, angular velocities of the vortices are primarily due to the localized rotation of the vortex structures associated with the wake instability. In this context, it may be mentioned that the wake structure is entirely different for both the streamwise and transverse rotation rates. As in the former case, the sphere rotation influences the local motion of the wake vortices, which experience near-wake twisting of the vortex filaments. In the latter, the wake instability triggers its motion, and the flow is continuously drawn upwards toward the advancing side, resulting in a large-scale shedding pattern. That is essentially reflected in the magnitude of wake fluctuations, which we quantify by the rms of lift coefficient (C_y') in Fig. 18(b). For increasing Ω, the fluctuating force coefficient increases monotonically in accordance with the increasing amplitude response shown
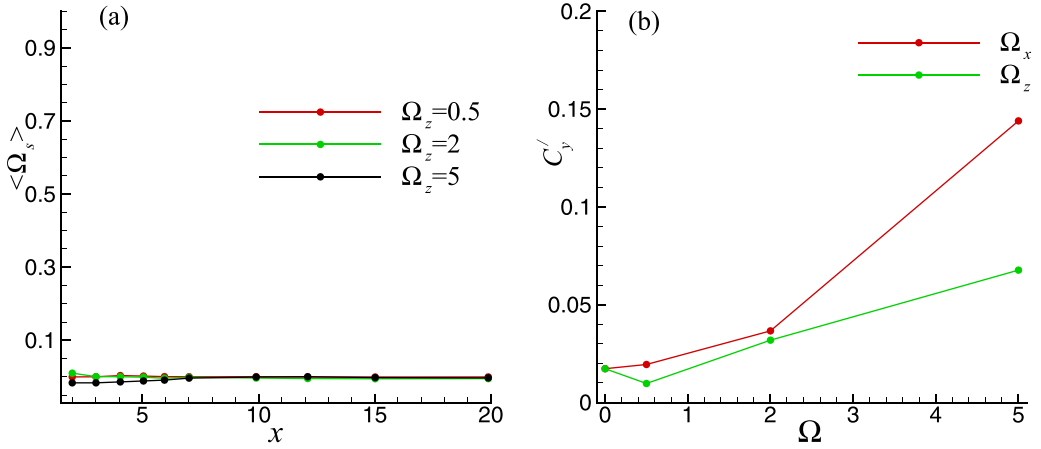
FIG. 18. (a) Functional variations of time average normalized angular velocity at various transverse (y-z) planes for different transverse rotation rates. (b) Dependence of the rms lift coefficient (C_y') with the streamwise and transverse rotation rates.

in Fig. 13. The trend of C_y' with Ω is similar to the one reported in Poon *et al.* [24]. Interestingly, it appears that increasing transverse rotation decreases the fluctuating component of the lift force, leading to a decrease in the oscillation amplitudes of the vortices. This observation is consistent with the earlier experimental results on a transversely rotating sphere [41]. In general, the peak magnitude of C_y' for $\Omega_z = 5$ is significantly smaller [$\mathcal{O}(10^{-2})$] as compared to $\Omega_x = 5$. We attribute this observation to the increased roll-up of the shear layers into randomly distributed vortex loops and contrails, which eventually trigger flow fluctuations and corresponding enhancements in C_y' magnitudes.

To obtain more insights, in Fig. 19, we plot the variations of f_Ω/f_s at different streamwise locations for various Ω_z. For all Ω_z, the turning motion of the sphere yields low-frequency rotation of the near wake vortices. As expected, the motion is asynchronous and becomes more asynchronous
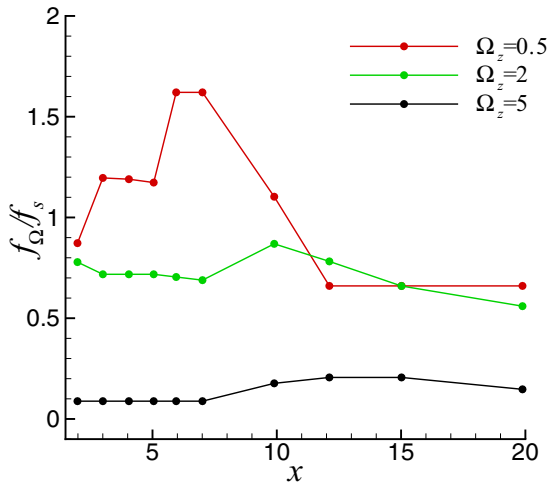

FIG. 19. Variation of the normalized angular frequency of the vortices, f_Ω/f_s as a function of Ω_z at various streamwise stations.
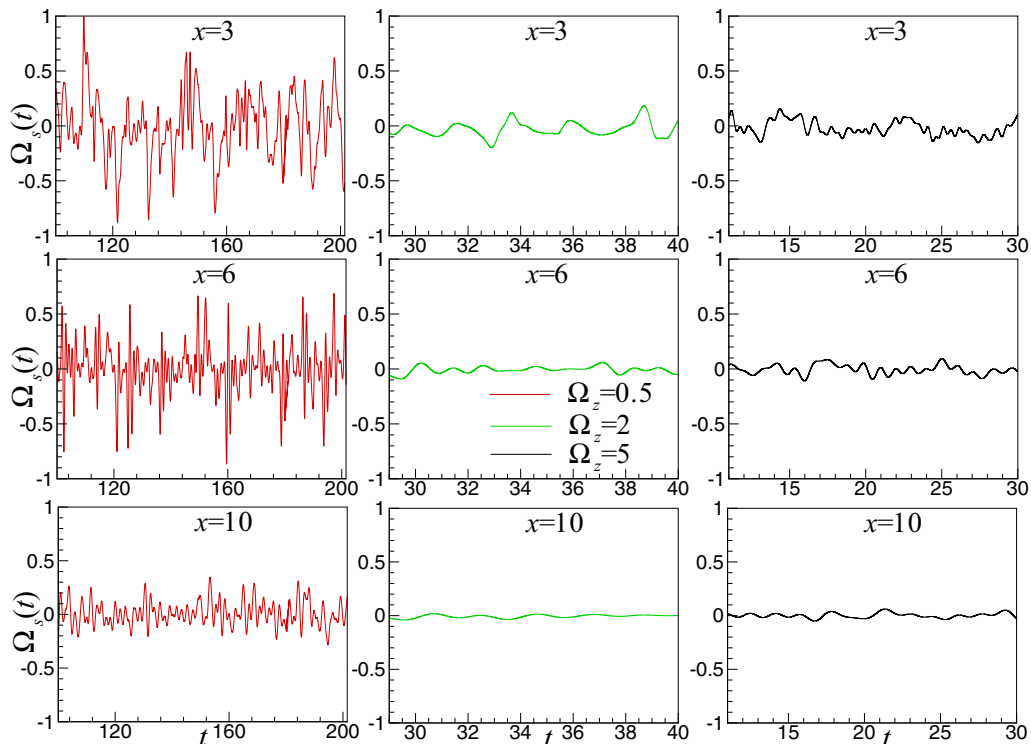
FIG. 20. Time histories of normalized angular velocities with the angular velocity of the sphere at different streamwise locations for various Ω_z.

with increasing Ω_z. Similarly to the one observed in Fig. 16, the vortices at lower Ω_z rotate at a higher frequency at different downstream stations. Although f_Ω/f_s settles at a constant value in the far wake. We observe a discontinuous jump in f_Ω/f_s curve in the near wake around $x \approx 5$ for $\Omega_z = 0.5$. Such a trend is due to the higher magnitudes of the angular velocities of the horseshow vortex structures just after its detachment, which eventually triggers the linear velocity of the vortices. Notice that for higher Ω_z, such discontinuity in the f_Ω/f_s variation is not discerned. We observe a marginal variation in f_Ω/f_s up to the far wake saturation. Therefore the low and high rotation rates display quite a different evolution of the wake. The former exhibits periodic shedding of coherent horseshoe vortices, while the latter show random roll-up of the structures advancing upstream of the sphere to yield top-heavy shear layers. As a result, the angular motion of the downstream vortices does not produce any local change in their frequency levels. This behavior is further revealed in the time histories of the normalized angular velocities at various downstream locations.

Figure 20 shows the time trace of the $\Omega_s(t)$ at different streamwise stations for various Ω_z. As the figure shows, the normalized angular velocity signals appear symmetric as the sphere rotates from the advancing to the retreating side. The overall signature of the $\Omega_s(t)$ contains quasiperiodic behavior. The lower rotational speed of the sphere induces larger Ω_s with a symmetric variation about $\Omega_s(t) = 0$. The amplitudes of oscillations are maximum in the near wake and decay to a minimum in the far wake locations. Compared to the lower rotational speed, the time evolutions of $\Omega_s(t)$ at $\Omega_z = 2$ show low-amplitude oscillations. The time histories of $\Omega_s(t)$ at all x locations are almost symmetric about $\Omega_s(t) = 0$. A similar trend is also discerned at $\Omega_z = 5$. Notably, the far wake ($x = 10$) shows nearly marginal variations in $\Omega_s(t)$. As we have seen, the turning motion of the sphere at higher rotation rates causes upstream shedding of the vortices, which in turn results in

an azimuthal stretching of the wake into numerous negative and positive vorticity cells with smaller circulation loops. In the far stream, owing to the wake instabilities, the circulation loops nullify each other to yield a few numbers of vorticity cells. That, in turn, leads to a gradual reduction in their angular velocities. We further note that the vortices at all downstream planes undergo clockwise and counterclockwise motions in each case of the rotational speeds. Therefore, it seems reasonable to argue that the added feature of the clockwise motions of the vorticities essentially cancels the equal magnitude of counterclockwise motion and culminates to trivial magnitudes of $\langle \Omega_s \rangle$, shown in Fig. 18(a). This is in contrast to the situation during the streamwise rotation of the sphere, where the angular velocity of the vortices is mostly counterclockwise (Fig. 17).

IV. CONCLUSIONS

We have studied the effect of streamwise (Ω_x) and transverse (Ω_z) rotation on the uniform flow past a sphere at Re = 500 for varying dimensionless rotation rates $\Omega_x, \Omega_z = 0.5, 2, 5$. In particular, we have compared the results with a stationary sphere. By studying the unsteadiness of the flow structure, we have found the generation of two intertwined spiral vortices at $\Omega_x = 0.5$. For $\Omega_x \geqslant 2$, the vortex structures form threads and, in the near wake, fragment into multiple vortex filaments. In the downstream end, the streamwise vortices bifurcate into large-scale structures for $\Omega_x = 5$. Moreover, the intense rotation of the sphere yields thinning of the shear layer, which then rolls up very close to the sphere's surface and discharges patches of negative and positive vorticity cells.

Our computations further uncovered a single-sided shedding of the hairpin structure at $\Omega_z = 0.5$. For increasing Ω_z from 0.5 to 2, the wake becomes asymmetric, and in the near wake, we found the deformation of vortex structures into multiple smaller-scale vortex filaments. At $\Omega_z = 5$, the vortex structures deflect toward the advancing side of the sphere, and the wake topology becomes complex, comprising strongly attached stretched hairpins. The shear layers become unstable, leading to upstream shedding of the vortices. In the downstream, we observe the transverse expansion of the wake owing to the bifurcation of the rolled-up positive and negative vortices into a twin jet-type flow pattern. We have computed the absolute magnitude of time-averaged vorticity ($\langle \omega \rangle$) at a streamwise plane to mark how deep the effects of streamwise and transverse rotations penetrate in the x direction. The $\langle \omega \rangle$ data for a stationary sphere nearly collapse with those for $\Omega_x, \Omega_z = 0.5$. In contrast, the shed vortices experience maximum forced-rotation-induced circulation at higher rotation rates.

The transient evolution of the vortical structures in a complete rotation cycle show absence of vortex shedding for $\Omega_x = 0.5$. In contrast, for $\Omega_z = 0.5$, we observe one-sided shedding of hairpin vortices in the near wake. The far wake shows a ringlike vortex structure. At $\Omega_x = 2$, the shear layers at the sphere's surface undergo successive stretching and then form hairpin vortices that shed bidirectionally in the far wake. The wake appears to be blunt shaped, which hardly rotates during successive instances of the rotation cycle. On the other hand, at $\Omega_z = 2$, the separation points advance upstream, causing roll-up of vortex loops randomly from the advancing side in various directions. The wake cannot cope with the sphere's rotation, rendering the downstream structures to retain their topology at various instances of the rotation cycle. The line-time reconstruction of v signals along x shows the flapping of shear layers at low rotation rates.

We have presented a technique for identifying the downstream vortex trajectories along various y-z planes. For $\Omega_x = 0.5$, the near wake trajectories follow a circular path, whereas, in the far wake, it settles at a larger radius. We have observed that the local rotation center of the near-wake vortical structures cannot cope with high rotational speeds, and fluid particles partially follow the consequences of solid-body rotation. In turn, fluid particles closer to the wake boundaries move faster than the particles preceding them, resulting in curved vortex trajectories. However, at $\Omega_x = 5$, a higher degree of mixing of the fluid particles in the near wake reduces localized rotation of the vortex trajectories, whereas the far wake vortex centers settle along the radial lines. Further, the vortex trajectories are symmetrically distributed at all transverse planes for $\Omega_z = 0.5$. The vortex centers move toward the negative z axis owing to the fluid motion along the axis of rotation.

However, for $\Omega_z = 5$, the trajectories are distributed symmetrically about the $\pm z$ axis. The phase diagrams of drag and lift change irregularly for increasing rotational speeds and has a preferred bias toward both negative and positive C_y axis. Notably, regardless of the direction of rotations, a rotating sphere always experiences a positive drag.

As the sphere rotates, its rotational inertia does not penetrate far in the wake. We have revealed such effects by computing the area average angular velocity at any y-z plane. For $\Omega_x = 0.5$, the near wake vortices at $x = 2$ could cope with the sphere's rotation and marginally decreases for $\Omega_x = 2$. Most of the sphere's rotational speed is lost for $\Omega_x = 5$. We have defined the penetration depth (δ_p) as the downstream distance for which 10% of the sphere's angular velocity is preserved by the downstream vortices. The normalized dominant azimuthal frequency (f_Ω/f_s) shows the asynchronous rotation of the vortex structures at different downstream stations. We found low-frequency rotation in the near wake at $\Omega_x = 0.5$, indicating torsion of the vortex structures. However, at higher rotational speeds, f_Ω/f_s variation yields a plateau region for $\Omega_x = 2, 5$. We have identified near wake, transition/plateau, and saturation/far-wake regions from the f_Ω/f_s distribution. The normalized angular velocity ($\Omega_s(t)$) in the near wake is periodic and becomes quasiperiodic for increasing Ω_x. For $\Omega_x = 0.5$, $\Omega_s(t) > 0$, however its changes sign alternatively for increasing Ω_x.

The effect of transverse rotation has a marginal influence on the rotation of the downstream vortices. The wake instability triggers the motion of the vortices, which are drawn toward advancing side of the sphere, ensuing a large-scale shedding pattern. The rms of the lift force increases with increasing Ω, although it is always lower during transverse rotation. We found that the transverse rotation of the sphere exhibits low-frequency rotation of the near wake vortices for all Ω_z. The motion is asynchronous, and its asynchronicity triggers with increasing Ω_z. The normalized angular velocity signals are symmetric and display quasiperiodic behavior. Oscillation amplitudes of $\Omega_s(t)$ at higher Ω_z are lower and show minimal variations in the far wake. Further, the angular velocity of the vortices is counterclockwise during the streamwise rotation of the sphere, whereas the transverse rotation yields clockwise and counterclockwise motions.

[1] P. Ern, F. Risso, D. Fabre, and J. Magnaudet, Wake-induced oscillatory paths of bodies freely rising or falling in fluids, Annu. Rev. Fluid Mech. **44**, 97 (2012).

[2] F. Auguste and J. Magnaudet, Path oscillations and enhanced drag of light rising spheres, J. Fluid Mech. **841**, 228 (2018).

[3] M. Passmore, S. Tuplin, A. Spencer, and R. Jones, Experimental studies of the aerodynamics of spinning and stationary footballs, Proc. Inst. Mech. Engrs C. **222**, 195 (2008).

[4] G. Robinson and I. Robinson, The motion of an arbitrarily rotating spherical projectile and its application to ball games, Phys. Scr. **88**, 018101 (2013).

[5] P. Shi and R. Rzehak, Lift forces on solid spherical particles in unbounded flows, Chem. Engng Sci. **208**, 115145 (2019).

[6] Z.-G. Feng and S. Musong, Direct numerical simulation of heat and mass transfer of spheres in a fluidized bed, Powder Technol. **262**, 62 (2014).

[7] S. I. Rubinow and J. B. Keller, The transverse force on a spinning sphere moving in a viscous fluid, J. Fluid Mech. **11**, 447 (1961).

[8] H. Schlichting, *Boundary Layer Theory* (McGraw–Hill, New York, 1960), pp. 176–206.

[9] S. Luthander and A. Ryberg, Experimentelle untersuchungen uber den luftwiderstand bei einer um eine mit der windrichtung parallele achse rotierenden kugel, Phys. Z **36**, 552 (1935).

[10] N. Hoskin, *Fifty Years of Boundary Layer Research* (Braunschweig, 1955), pp. 127–131.

[11] Y. Tsuji, Y. Morikawa, and O. Mizuno, Experimental measurement of the magnus force on a rotating sphere at low reynolds numbers, Trans. ASME **107**, 484 (1985).

[12] B. D. Tri, B. Oesterle, and F. Deneu, Premiers resultats sur la portance d'une sphere en rotation aux nombres de reynolds intermediaies, C. R. Acad. Sci. Paris II **311**, 27 (1990).

[13] B. Oesterlé and B. Dinh, Experiments on the lift of a spinning sphere in a range of intermediate reynolds numbers, Exp. Fluids **25**, 16 (1998).

[14] J. B. Barlow and M. J. Domanski, Lift on stationary and rotating spheres under varying flow and surface conditions, AIAA J. **46**, 1932 (2008).

[15] T. Kray, J. Franke, and W. Frank, Magnus effect on a rotating sphere at high reynolds numbers, J. Wind Engng Indust. Aerodyn. **110**, 1 (2012).

[16] J. Kim, H. Choi, H. Park, and J. Y. Yoo, Inverse magnus effect on a rotating sphere: When and why, J. Fluid Mech. **754**, R2 (2014).

[17] M. Skarysz, J. Rokicki, S. Goujon-Durand, and J. E. Wesfreid, Experimental investigation of the wake behind a rotating sphere, Phys. Rev. Fluids **3**, 013905 (2018).

[18] R. Kurose and S. Komori, Drag and lift forces on a rotating sphere in a linear shear flow, J. Fluid Mech. **384**, 183 (1999).

[19] H. Niazmand and M. Renksizbukut, Surface effects on transient three-dimensional flows around rotating spheres at moderate reynolds numbers, Comput. Fluids **32**, 1405 (2003).

[20] D. Kim and H. Choi, Laminar flow past a sphere rotating in the streamwise direction, J. Fluid Mech. **461**, 365 (2002).

[21] D. Kim, Laminar flow past a sphere rotating in the transverse direction, J. Mech. Sci. Technol. **23**, 578 (2009).

[22] M. Giacobello, A. Ooi, and S. Balachandar, Wake structure of a transversely rotating sphere at moderate reynolds numbers, J. Fluid Mech. **621**, 103 (2009).

[23] B. Pier, Periodic and quasiperiodic vortex shedding in the wake of a rotating sphere, J. Fluids Struct. **41**, 43 (2013).

[24] E. K. W. Poon, A. S. H. Ooi, M. Giacobello, G. Iaccarino, and D. Chung, Flow past a transversely rotating sphere at reynolds numbers above the laminar regime, J. Fluid Mech. **759**, 751 (2014).

[25] J. Dobson, A. Ooi, and E. K. W. Poon, The flow structures of a transversely rotating sphere at high rotation rates, Comput. Fluids **102**, 170 (2014).

[26] E. K. W. Poon, A. S. H. Ooi, M. Giacobello, and R. C. Cohen, Laminar flow structures from a rotating sphere: Effect of rotating axis angle, Int. J. Heat Fluid Flow **31**, 961 (2010).

[27] E. K. W. Poon, A. S. H. Ooi, M. Giacobello, and R. C. Cohen, Hydrodynamic forces on a rotating sphere, Int. J. Heat Fluid Flow **42**, 278 (2013).

[28] M. Lorite-Díez and J. I. Jiménez-González, Description of the transitional wake behind a strongly streamwise rotating sphere, J. Fluid Mech. **896**, A18 (2020).

[29] J. Sierra-Ausín, M. Lorite-Díez, J. I. Jiménez-González, V. Citro, and D. Fabre, Unveiling the competitive role of global modes in the pattern formation of rotating sphere flows, J. Fluid Mech. **942**, A54 (2022).

[30] F. W. Roos and W. W. Willmarth, Some experimental results on sphere and disk drag, AIAA J. **9**, 285 (1971).

[31] T. A. Johnson and V. C. Patel, Flow past a sphere up to a reynolds number of 300, J. Fluid Mech. **378**, 19 (1999).

[32] S. Taneda, Experimental investigation of the wake behind a sphere at low reynolds numbers, J. Phys. Soc. Jpn. **11**, 1104 (1956).

[33] D. Pan and T. T. Shen, Computation of incompressible flows with immersed bodies by a simple ghost cell method, Int. J. Numer. Methods Fluids **60**, 1378 (2009).

[34] A. K. De, A diffuse interface immersed boundary method for convective heat and fluid flow, Int. J. Heat Mass Transfer **92**, 957 (2016).

[35] A. K. De, A diffuse interface immersed boundary method for complex moving boundary problems, J. Comput. Phys. **366**, 226 (2018).

[36] A. K. De and S. Sarkar, Spatial wake transition past a thin pitching plate, Phys. Rev. E **104**, 025106 (2021).

[37] A. K. De and S. Sarkar, Dependence of wake structure on pitching frequency behind a thin panel at $Re = 1000$, J. Fluid Mech. **924**, A33 (2021).

[38] J. Jeong and F. Hussain, On the identification of a vortex, J. Fluid Mech. **285**, 69 (1995).

[39] S. Behara, I. Borazjani, and F. Sotiropoulos, Vortex-induced vibrations of an elastically mounted sphere with three degrees of freedom at $Re = 300$: Hysteresis and vortex shedding modes, J. Fluid Mech. **686**, 426 (2011).

[40] D. Virk, F. Hussain, and R. M. Kerr, Compressible vortex reconnection, J. Fluid Mech. **304**, 47 (1995).

[41] A. Sareen, J. Zhao, D. L. Jacono, J. Sheridan, K. Hourigan, and M. C. Thompson, Vortex-induced vibration of a rotating sphere, J. Fluid Mech. **837**, 258 (2018).

[42] L. Graftieaux, M. Michard, and N. Grosjean, Combining PIV, POD and vortex identification algorithms for the study of unsteady turbulent swirling flows, Meas. Sci. Technol. **12**, 1422 (2001).